



**HAL**  
open science

## Satellite-derived shoreline detection at a high-energy meso-macrotidal beach

Bruno Castelle, Gerd Masselink, Tim Scott, Christopher Stokes, Aikaterini Konstantinou, Vincent Marieu, Stéphane Bujan

► **To cite this version:**

Bruno Castelle, Gerd Masselink, Tim Scott, Christopher Stokes, Aikaterini Konstantinou, et al.. Satellite-derived shoreline detection at a high-energy meso-macrotidal beach. *Geomorphology*, 2021, 383, pp.107707. 10.1016/j.geomorph.2021.107707 . hal-03411192

**HAL Id: hal-03411192**

**<https://hal.science/hal-03411192>**

Submitted on 2 Nov 2021

**HAL** is a multi-disciplinary open access archive for the deposit and dissemination of scientific research documents, whether they are published or not. The documents may come from teaching and research institutions in France or abroad, or from public or private research centers.

L'archive ouverte pluridisciplinaire **HAL**, est destinée au dépôt et à la diffusion de documents scientifiques de niveau recherche, publiés ou non, émanant des établissements d'enseignement et de recherche français ou étrangers, des laboratoires publics ou privés.

# 1 **Satellite-derived shoreline detection at a high-energy meso-macrotidal beach**

2 Bruno Castelle<sup>1,2</sup>, Gerd Masselink<sup>3</sup>, Tim Scott<sup>3</sup>, Christopher Stokes<sup>3</sup>, Aikaterini Konstantinou<sup>3</sup>, Vincent  
3 Marieu<sup>1,2</sup>, Stéphane Bujan<sup>1,2</sup>

4 <sup>1</sup>CNRS, UMR EPOC, Pessac, France

5 <sup>2</sup>Université de Bordeaux, UMR EPOC, Pessac, France

6 <sup>3</sup>Coastal Processes Research Group, School of Biological and Marine Sciences, University of Plymouth,  
7 Plymouth, UK

8 Corresponding author: [bruno.castelle@u-bordeaux.fr](mailto:bruno.castelle@u-bordeaux.fr)

9

## 10 **Highlights**

- 11 • 35 years of satellite-derived shorelines at a high-energy tidal beach are analysed
- 12 • Satellite-derived shoreline proxies are compared with 10 years of field data
- 13 • A new approach using wave runup and a threshold on total water level is proposed
- 14 • The approach halves shoreline error and doubles the number of usable images

## 15 **Abstract**

16 Publicly available satellite imagery can now provide multi-decadal time series of shoreline data from  
17 local to global scale, enabling analysis of sandy beach shoreline variability across a spectrum of  
18 temporal scales. Such data can, however, be associated with large uncertainties, particularly for  
19 beaches experiencing a large tidal range (> 2 m) and energetic incident waves. We use a decade of bi-  
20 monthly topographic surveys at the high-energy meso-macrotidal beach of Truc Vert, southwest  
21 France, and concurrent wave and water-level hindcast to investigate the uncertainties associated  
22 with satellite-derived time series of the shoreline position. We show that consideration of the water  
23 level and wave runup elevation are critical for accurately estimating waterline position and, in turn,  
24 shoreline position. At Truc Vert, including non-tidal water level residuals (e.g. wind-driven surge) and  
25 accounting for time- and elevation-varying beach slope for horizontal correction did not improve  
26 satellite-derived shoreline position. A new total water level threshold is proposed to maximize the  
27 number of usable images while minimizing errors. Accounting for wave runup and the new water  
28 level threshold at Truc Vert, the number of usable satellite images is doubled and shoreline position  
29 errors are at least halved compared to previous work at this site. Using the 1984-2019 reconstructed  
30 shoreline, we also show that the satellite-derived shoreline trends and interannual variability are in  
31 better agreement with field measurements. Although the approach proposed here needs to be

32 tested on other sites in different tidal/wave forcing environments with different morphological and  
33 sediment characteristics, we anticipate that it will improve the temporal and spatial description of  
34 shoreline change on most surf tidal beaches where accurate continuous water level and wave  
35 hindcasts and/or observations are available.

36 **Keywords:** shoreline change; long-term trend; satellite; wave runup

37

## 39 **1. Introduction**

40 Understanding and predicting shoreline change along sandy coasts is of paramount importance for  
41 coastal managers and policy-makers (Stive et al., 2002). Ambient (or background) long-term  
42 shoreline change is an essential and sometimes dominant component in models of future shoreline  
43 change due to sea-level rise (Vitousek et al., 2017; Vousdoukas et al., 2020; McCarroll et al., 2020).  
44 However, shoreline variability occurs across a wide range of time scales and it can be challenging to  
45 derive the ambient shoreline change unless very long data time series are available. Shorelines can  
46 dramatically erode within hours as a result of storm waves (Harley et al., 2017). At the other end of  
47 the spectrum, long-term, multi-decadal shoreline change is driven by various processes such as sea-  
48 level rise (Ranasinghe et al., 2012) and coastal sediment supply (Carter et al., 1987). In between,  
49 seasonal and interannual shoreline variability is primarily driven by changes in incident wave  
50 conditions (Dodet et al., 2019); however, in sectors adjacent to tidal inlets and estuary mouths,  
51 fluctuations in ebb-channel morphology can also drive shoreline variability (O'Connor et al., 2011).  
52 Anthropogenic forcing, such as beach nourishments or implementation of hard structures that  
53 disturb sediment pathways may also have a profound impact on shoreline variability (Turner, 2006).  
54 A core issue to improve our understanding and ability to predict shoreline change is therefore to  
55 monitor shoreline change at the highest possible frequency and the longest possible time scale on a  
56 large range of sandy environments representative of the natural variability (Splinter et al., 2013;  
57 Ibaceta et al., 2020; Toimil et al., 2020).

58 There is a wealth of coastal monitoring techniques employed to survey beach morphology and derive  
59 shoreline change. These topographic surveys are often performed by means of GNSS surveys  
60 (Baptista et al., 2008). Large-scale GNSS coastal monitoring programs based on widely spaced beach  
61 profiles adequately distributed along 10s to 100s kilometres are scarce (Wijnberg and Terwindt,  
62 1995; Ludka et al., 2019). Instead, most coastal monitoring programs focus on a single site through  
63 representative profiles (e.g., Lee et al., 1998; Suanez et al., 2012; Turner et al., 2016) or detailed  
64 digital elevation models (DEMs) along 100s to 1000s of metres (e.g., Stokes et al., 2015; Castelle et  
65 al., 2017a), which are typically surveyed monthly or bimonthly. On similar lengths of coastline, the  
66 daily shoreline proxy can be inferred from permanent video stations at reasonably low cost over  
67 years to decades (e.g., Harley et al., 2011), although associated with lower accuracy.  
68 Photogrammetry based on UAV images has also recently emerged as a promising tool to monitor  
69 100s to 1000s metres of coast at high spatial resolution (e.g., Laporte-Fauret et al., 2019). Larger  
70 scale, say 10s to 100s of kilometres, coastal monitoring programs are typically based on Lidar surveys

71 (Le Mauff et al., 2018; Nicolae Lerma et al., 2019). However, such surveys are costly and have low  
72 repeat frequencies. They are therefore difficult to maintain on the long-term and do not provide  
73 insight into seasonal variability.

74 Publicly available satellite imagery can now be used at no cost to provide short-term to multi-decadal  
75 shoreline data from local to global scale using a variety of techniques (e.g., Garcia-Rubio et al., 2015;  
76 Liu et al., 2017; Qiao et al., 2018; Douarte et al., 2018; Toure et al., 2019). Long-term (> 30 yrs) global  
77 estimation of shoreline erosion and accretion were recently proposed by Luijendijk et al. (2018) and  
78 Mentaschi et al. (2018). Although these studies provided unprecedented global insight into shoreline  
79 change, a detailed inspection of the satellite-derived trends computed in Luijendijk et al. (2018) at  
80 many high-energy and/or meso to macrotidal beaches reveals that many of these trends are not  
81 supported by field data and empirical evidence. Although trends appear reliable in sectors where  
82 dramatic change is observed (Luijendijk et al., 2018), the discrepancies are obvious primarily in slowly  
83 evolving sectors, say less than several metres per year, and at sites with a large intra- and inter-  
84 annual shoreline variability. A more accurate assessment of shoreline change rates is therefore a  
85 necessary requirement to develop reliable identification of a global typology of accreting, stable and  
86 eroding shores. Furthermore, these computed historical trends can be extrapolated and combined  
87 with debatable sea-level-rise impact rule to conclude on shoreline position by the end of the century  
88 and potential extinction of half of the world's beaches (Vousdoukas et al., 2020). In addition to  
89 addressing the limitations to this approach pointed out in Cooper et al. (2020), such pioneering  
90 projective work would gain in reliability by improving the historical shoreline trends, as well as  
91 including the effects of potential multi-decadal variability.

92 Vos et al. (2019a) recognised issues with detecting shorelines using satellite data on dissipative  
93 beaches and sites experiencing a large tidal range. After Liu et al. (2017) who showed that tidal effect  
94 correction improves satellite-derived shoreline errors, Vos et al. (2019b) tested a tidal correction at a  
95 meso-macrotidal site by using a time-invariant characteristic beach face slope and only using images  
96 captured at higher stages of the tide. This decreased the shoreline position error by 15 m. No  
97 significant improvement in their error statistics was found using slope measurements from the  
98 closest survey compared to using the single time-invariant slope value. However, the effects of wave  
99 runup on water level at the coast, which can cause large horizontal translation of the waterline and  
100 shoreline position under moderate- to high-energy breaking waves, was not considered. Other  
101 sources of errors associated with satellite-derived shorelines can also arise, such as for instance  
102 through issues with geo-referencing (Schubert et al., 2017) and incorrect delineation of the  
103 water/sand interface (Toure et al., 2019).

104 Overall, improving satellite-derived shoreline positions and, in turn, shoreline trends is critical to  
105 more accurately discriminate accreting, stable and eroding beaches, and to reduce uncertainties in  
106 future shoreline change projections in the frame of climate change, both locally and globally. In this  
107 paper, we address satellite-derived shoreline evolution at the high-energy and meso-macrotidal  
108 beach of Truc Vert, southwest France, using the out-of-the-box open access python-based CoastSat  
109 toolkit (Vos et al., 2019a, 2019b). We explore if including astronomical tide, non-tidal water level  
110 residuals, wave action and local beach slope can reduce shoreline position uncertainties, and  
111 therefore lead to an improved assessment of long-term trends and interannual variability. We also  
112 investigate the value of increasing the number of satellite images in the analysis. These results have  
113 strong implications from the perspective of global long-term trend computations and further  
114 extrapolation until the end of the century, as well as for the assessment of interannual shoreline  
115 variability on beaches.

## 116 **2. Study area**

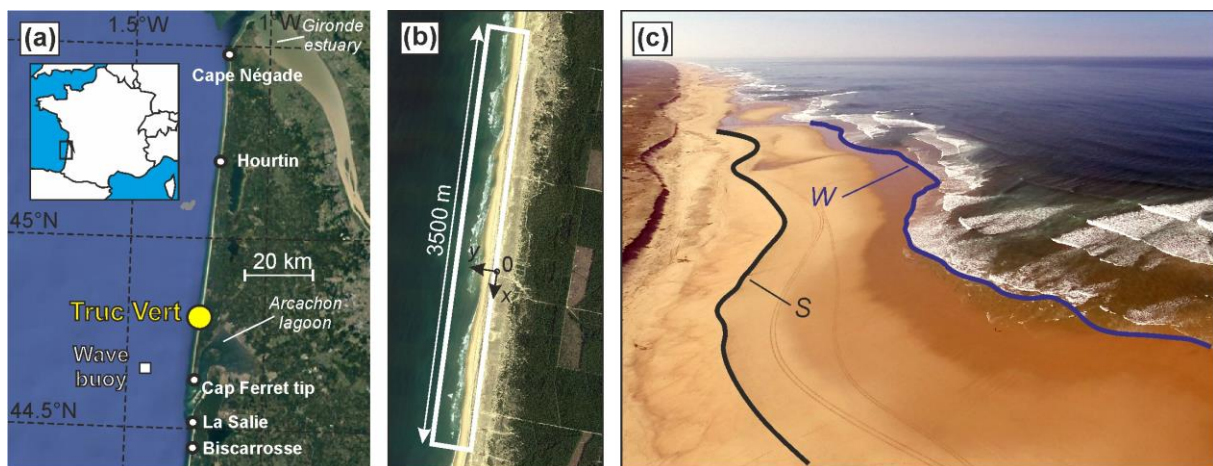
117 The study site is located in southwest France, extending c. 140 km from the Gironde estuary in the  
118 north to Biscarrosse in the south, with a focus on Truc Vert beach (Figure 1a). This sandy coast  
119 comprises a large beach-dune system that is only interrupted by the Arcachon lagoon inlet.

120 The wave climate at these latitudes along the Atlantic coast of Europe is generated in the North  
121 Atlantic Ocean, predominantly by eastward-tracking extra-tropical cyclones. Wave conditions at Truc  
122 Vert, described below, are based on a numerical wave hindcast detailed in Section 3.2. The incident  
123 wave conditions are strongly seasonally modulated with the monthly-averaged significant wave  
124 height  $H_s$ , peak wave period  $T_p$  and angle of wave incidence  $\theta$  ranging, respectively, from 1.1 m, 8.8 s  
125 and  $297^\circ$  in summer, to 2.4 m, 12.1 s and  $287^\circ$  in winter (Figure 2a–c). Thus, larger and longer waves  
126 with a more western incidence occur in winter compared to summer. Winter wave activity shows a  
127 strong interannual variability, with moderate winters alternating with extreme winters characterised  
128 by significant spatial and temporal storm clustering (Masselink et al., 2016). High-energy winters  
129 occur as a result of the intensification and southward shift of Azores high / Icelandic low dipole,  
130 which is strongly correlated with the West Europe Pressure Anomaly climate index and weakly  
131 associated with the North Atlantic Oscillation (Castelle et al., 2017b).

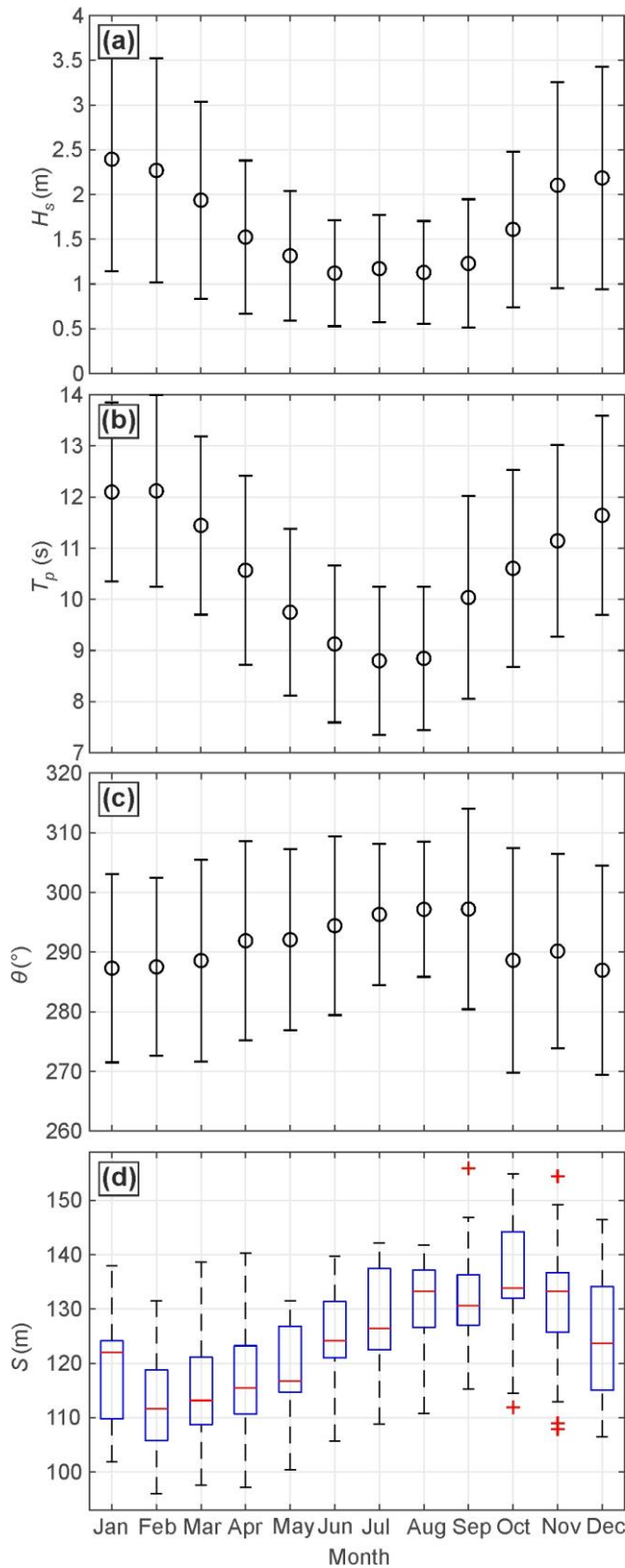
132 The coast is meso-macrotidal with an annual mean spring tidal range of 3.7 m and a largest  
133 astronomical tidal range of c. 5 m (Castelle et al., 2017a). Nearshore tide-driven currents are intense  
134 ( $> 1$  m/s) in the vicinity of the Gironde estuary mouth and Arcachon tidal inlet, and are negligible ( $<$   
135  $0.2$  m/s) compared to wave-driven currents on the open coast that can well exceed 1 m/s in rip-cell  
136 circulation of under energetic obliquely incident waves.

137 The beach sediment consists of medium quartz sand with a median grain size of c. 0.35 mm and a  
138 large spatial variability (Gallagher et al., 2011). Except adjacent to the tidal inlet and estuary mouths,  
139 beaches are morphodynamically intermediate, but with a double-bar system. The subtidal outer bar  
140 is modally crescentic and a modally transverse bar-rip system characterises the intertidal inner bar  
141 system. The inner and outer mean rip spacing is approximately 400 and 700 m, respectively, with  
142 large spatial and temporal variability (Castelle et al., 2007; Almar et al., 2010).

143 Analysis of georeferenced aerial photographs since 1950 showed a large spatial variability of  
144 shoreline change within the study area (Castelle et al., 2018). Maximum shoreline dynamics are  
145 observed along the sectors adjacent to the Gironde Estuary mouth and Arcachon inlet (Figure 1a),  
146 with erosion and accretion alternating on the timescale of decades. In the northern sector near Cape  
147 Négade (Figure 1a), the mean erosion rate is largest at c. 5 m/yr, with a quasi-steady trend. Mean  
148 erosion rate decreases southwards to 1–2 m/yr at approximately 30 km south of Hourtin (Figure 1a).  
149 Further south, the coast has been relatively stable over the last 70 years along a c. 20-km long sector.  
150 This sector comprises Truc Vert beach (Figure 1a), of which topographic data will be used herein to  
151 compare satellite-derived shoreline dynamics.



152  
153 Figure 1. (a) Location map, (b) survey region and reference frame used at Truc Vert beach and (c)  
154 aerial view of Truc Vert beach taken between low and mid tide, with indication of water level ( $W$ )  
155 position and visual estimate of the 1.5-m shoreline proxy  $S$ , which is the optimal shoreline proxy at  
156 Truc Vert (photo: Vincent Marieu).



157

158 Figure 2. Monthly wave statistics offshore of Truc Vert for 2005–2020: (a) significant wave height  $H_s$ ;

159 (b) peak wave period  $T_p$ ; (c) angle of wave incidence  $\theta$ ; and (d) cross-shore position of the

160 alongshore-averaged 1.5-m elevation shoreline proxy at Truc Vert  $S$ . Circles and vertical error bars in

161 (a–c) indicate the monthly mean and the  $\pm 1$  monthly standard deviation, respectively. The central

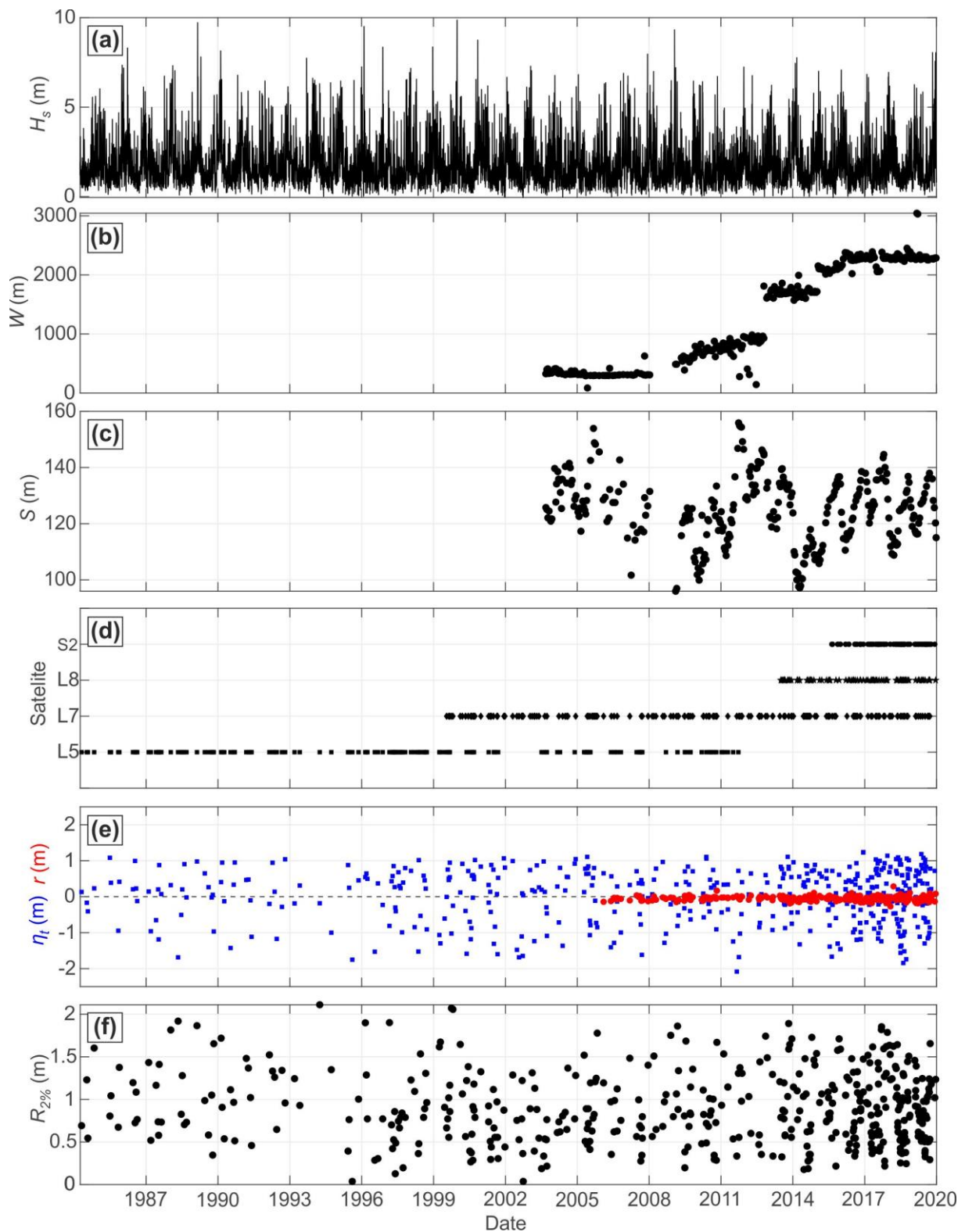


162 horizontal mark in (d) indicates the median and the top and bottom edges of the blue boxes indicate  
163 the 25<sup>th</sup> and 75<sup>th</sup> percentiles, respectively. Maximum whisker length extends up to 1.5 times the  
164 interquartile range. Data points beyond these whiskers are considered as outliers and are displayed  
165 individually as red crosses.

### 166 **3. Data and methods**

#### 167 **3.1 Truc Vert beach surveys**

168 A continuous beach survey program has been operational since 2003 at Truc Vert. The resulting  
169 monthly to bi-monthly beach morphology dataset is detailed and made available in Castelle et al.  
170 (2020). The alongshore coverage of the surveys increased over time, exceeding 600 m in 2009 before  
171 stabilizing at c. 2200 m since early 2016 (Figure 3b). Figure 3c shows the time series of 1.5-m  
172 elevation shoreline proxy cross-shore position  $S_{1.5m}$ , which has been used as the primary shoreline  
173 proxy in previous studies (e.g., Castelle et al., 2014; Splinter et al., 2014) as it best correlates with the  
174 beach-dune volume (Robinet et al., 2016). It is defined as the intersection of the alongshore-  
175 averaged profile with the 1.5-m AMSL elevation datum, where AMSL is obtained at Truc Vert by  
176 subtracting 0.4 m from the French National Geodesic Service (NGF-IGN 69) height (Castelle et al.,  
177 2020). In line with earlier work (e.g., D'Anna et al., 2020), the shoreline shows large seasonal cycles  
178 with a typical amplitude of c. 30–40 m, with superimposed interannual variability of similar  
179 amplitude. In the following, only the topographic data collected from 2009 onwards, which extend  
180 more than 600 m alongshore, will be used for validation of local and alongshore-averaged satellite-  
181 derived waterline ( $\bar{X}$ ) and shoreline ( $\bar{S}$ ) positions.



182

183 Figure 3. Time series of: (a) significant wave height  $H_s$ ; (b) survey alongshore coverage  $W$ ; (c) cross-  
 184 shore location of the alongshore-averaged 1.5-m elevation shoreline proxy  $S$  computed from the  
 185 topographic surveys; (d) usable L5, L7, L8 and S2 satellite images after automatic and visual  
 186 inspection (see text for details); (e) astronomical tide  $\eta_t$  estimated from an harmonic analysis of

187 2006-2020 MARC hindcast, for which non-tidal residuals  $r$  were also extracted; and (f) runup  
188 elevation  $R_{2\%}$ . All values shown in (e,f) are given at the satellite flyover time.

### 189 **3.2 Wave and water level data**

190 There is no continuous wave buoy measurements nearby Truc Vert covering the 1984-2019 satellite  
191 image period. Instead we used a 26-year (1994–2019) time series of regional wave hindcast  
192 (Boudière et al., 2013; Michaud et al., 2015) at the grid point collocated with the Candhis directional  
193 wave buoy moored in c. 54 m depth southwest of Truc Vert (Figure 1a), showing excellent skill  
194 against interspersed buoy measurements (see Castelle et al., 2020 for details). To further extend the  
195 time series from 1994 back until the early 1980s when the first satellite images were acquired, we  
196 used the 1948–2015 wave hindcast described in Masselink et al. (2016), which was validated against  
197 the nearby Candhis wave buoy data in Castelle et al. (2014), although with poorer skill than with the  
198 1994-2019 regional wave model.

199 A 2006-2020 coastal model hindcast of water level (Pineau Guillou, 2013) validated at Truc Vert in  
200 Castelle et al. (2020) was used to estimate the water level at the coast. The astronomical tide  
201 component ( $\eta_t$ ) as well as the water level including non-tidal (atmospheric) residuals  $r$  ( $\eta_{ts} = \eta_t + r$ )  
202 were extracted all along the coast in c. 10 m depth. A harmonic analysis of the 2006-2020 MARC  
203 hindcast astronomical tide (no storm surge) was performed to extend the time series of  $\eta_t$  back until  
204 the early 1980s (Figure 3e).

205 Breaking waves are responsible for increased water level at the shoreline (Stockdon et al., 2006). We  
206 tested many set-up  $\zeta$  and runup  $R_{2\%}$  parametrizations, which will be discussed later in the paper.  
207 Based on preliminary tests and practical considerations, we used the runup formulation of Sénéchal  
208 et al. (2011), specifically calibrated at Truc Vert:

$$209 \quad R_{2\%} = 2.14 \tanh 0.4H_s \quad (1)$$

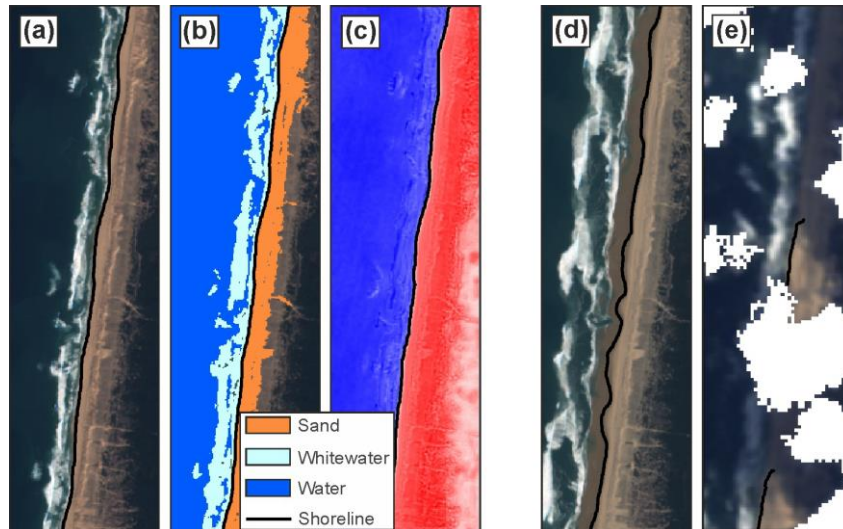
210 Contrary to many other runup parametrizations (e.g., Stockdon et al., 2006), Equation (1) implies that  
211  $R_{2\%}$  can be scaled using offshore wave height alone at Truc Vert. This is in line with previous  
212 observations on highly dissipative beaches (Ruessink et al., 1998; Ruggiero et al., 2001) when  
213 infragravity energy dominates runup.

214 Given that we also considered disregarding any water level variation ( $\eta = \eta_o = 0$ ), in total four  
215 combinations of water level  $\eta$  at the coast were considered: no water level variation ( $\eta_o$ );  
216 astronomical tide ( $\eta_t$ ); astronomical tide + surge ( $\eta_{ts}$ ); astronomical tide + surge + runup ( $\eta_{tsr}$ ).

### 217 **3.3 Publicly available satellite images and waterline detection algorithm**

218 We used the python toolkit CoastSat (Vos et al., 2019b) which is freely-available on GitHub  
219 (<https://github.com/kvos/CoastSat>). The overall approach is described in detail in Vos et al. (2019a).  
220 Briefly, the toolkit allows extracting waterlines from publicly available optical satellite data through  
221 Google Earth Engine. Landsat 5, 7 & 8 (L5, L7, L8, 30-m spatial resolution) and Sentinel-2 (S2, 10-m  
222 spatial resolution) images are retrieved to a user-defined region of interest before pre-processing to  
223 remove cloudy pixels and enhance spatial resolution. A generic waterline detection algorithm is then  
224 applied, consisting of two main steps: (1) an image classification into the four classes of 'sand',  
225 'water', 'white-water' and 'other' is performed based on a Neural Network classifier algorithm  
226 trained on five training sites along the New South Wales coast; and (2) a sub-pixel resolution border  
227 segmentation based on the Modified Normalized Difference Water Index (MNDWI), which is widely  
228 used to discriminate water from land features in many applications (Xu, 2006). Instead of a global  
229 threshold on the MNDWI, a refined threshold that best divides the specific 'sand' and 'water' pixels  
230 by maximizing the inter-class variance is used. It provides a more stable and robust waterline  
231 boundary through time (Vos et al., 2019a). A sub-pixel resolution contouring algorithm, referred to as  
232 Marching Squares (Cipolletti et al., 2012), is then used to compute and map the waterline  $W$ .

233 A CoastSat region was defined at Truc Vert, with Figure 4 showing an example Sentinel-2 satellite  
234 image (Figure 4a), the corresponding classified image (Figure 4b), MNDWI pixel values (Figure 4c) and  
235 the resulting waterline position. Although a total of 1178 satellite images were available at Truc Vert,  
236 many images were not useful. For example, more than half of the images were affected by clouds,  
237 which resulted in the automatic removal of 361 images exceeding 50% of cloud cover from the  
238 analysis. An additional 339 images were manually removed by visual inspection when the algorithm  
239 failed to depict shoreline position for a number of reasons, including: flawed detection of the  
240 water/sand limit due to a saturated intertidal domain (Figure 4d) and shadows cast by clouds  
241 affecting waterline detection (Figure 4e). Recent Coastsat toolkit development now allows manual  
242 adjustment of the waterline by shifting the MNDWI threshold in the MNDWI pixel intensity  
243 histogram. However, at the time of using the Coastsat toolkit in the frame of this study, such  
244 development was not available but will be addressed in future study. Based on a thorough visual  
245 inspection of the images by the operator, a total of 478 Landsat images (including post May 2003 L7  
246 images when Scan Line Corrector failed) and Sentinel images (213 since 2009) were therefore used  
247 hereafter at Truc Vert representing the period 1984–2019 (Figure 3d).



248

249 Figure 4. Outputs from the CoastSat tool of Vos (2019b): (a) RGB image of Truc Vert beach from S2  
 250 satellite on February 28, 2019; (b) output of image classification where each pixel is labelled as  
 251 ‘sand’, ‘water’, ‘white-water’ or ‘other’; (c) pseudocolor image of the MNDWI pixel values. Examples  
 252 of images manually disregarded in the analysis: (d) when the algorithm depicted the dry beach limit  
 253 instead of the waterline due to a saturated intertidal domain (S2 on April 19, 2018); (e) presence of  
 254 clouds and large casted shadow (L5 on February 23, 1998). In all panels, the black line indicates the  
 255 waterline detected by CoastSat.

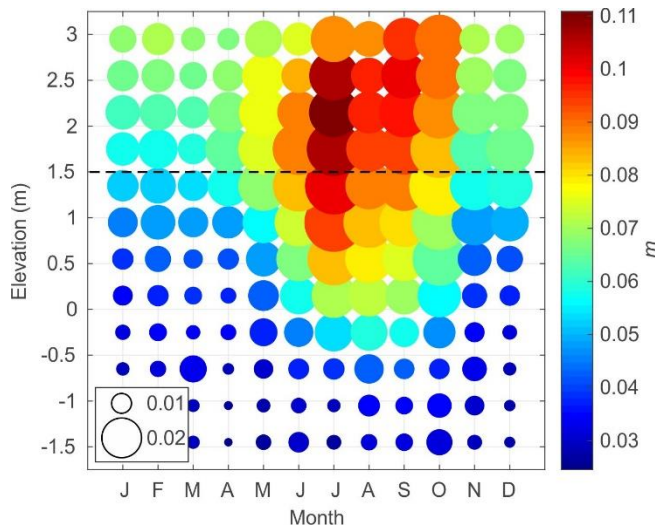
### 256 3.4 Shoreline position computations

257 The satellite-derived waterlines were transformed onto the local grid coordinate system. Given that  
 258 satellite images were taken for a wide range of water levels (Figure 3e) and our interest is in the  
 259 shoreline position  $S$ , waterline positions  $W$  were projected to 1.5 m AMSL, which is the most  
 260 relevant shoreline proxy at Truc Vert as it best correlates with beach-dune volume (Robinet et al.,  
 261 2016). A water-level correction was applied by translating horizontally the waterline  $W$  using a given  
 262 beach slope  $m$  and the water level at the coast  $\eta$  at the satellite flyover time:

$$263 \quad \Delta y = \frac{\eta - 1.5}{m} \quad (2)$$

264 where  $\Delta y$  is the cross-shore horizontal shift, positive onshore. The four water-level elevations  
 265 estimations given in Section 3.2 were tested. In addition, while a constant representative slope for  
 266 Truc Vert of  $m = 0.05$  was used in line with Vos et al. (2019a), a time- and elevation-dependant slope  
 267 was also tested here. For the latter, the Truc Vert beach surveys were used to compute the monthly  
 268 mean beach slope between the 1.5 m AMSL elevation and any elevation along the monthly-mean  
 269 profile (Figure 5). Beach slope computed from the 1.5 m AMSL elevation to any elevation ranging  
 270 between -1.5 m and + 3 m AMSL, with end-point slope varying from c. 0.02 to 0.11. Larger slopes are  
 271 observed at the upper part of the beach during summer, and more gentle slopes during winter and

272 along the lower part of the profile. Monthly beach slope, however, shows large interannual  
 273 variability (see large bubbles in Figure 5), particularly during summer at the upper part of the beach.



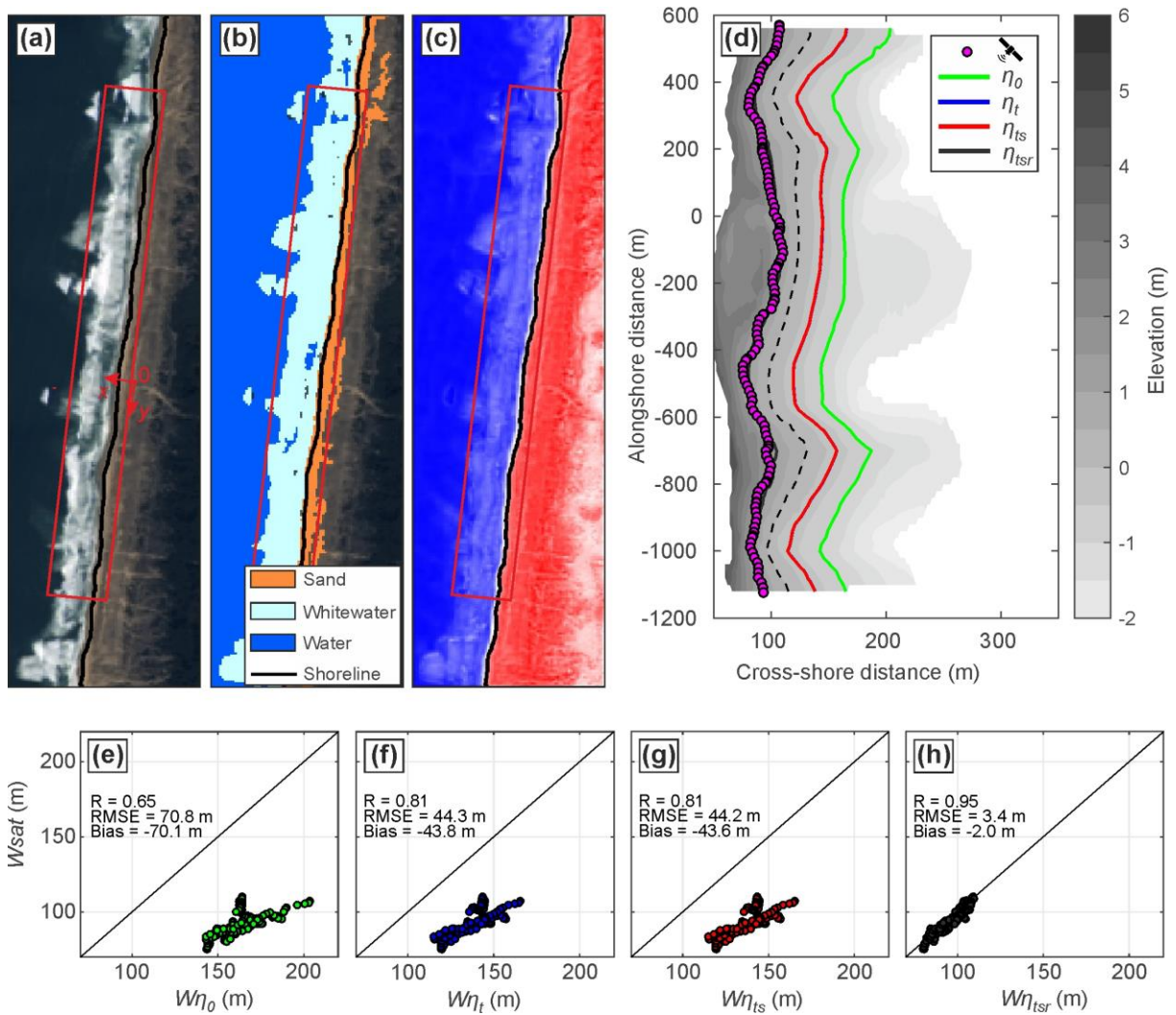
274  
 275 Figure 5. Monthly- and alongshore-averaged beach slope  $m$  between a given elevation and the 1.5 m  
 276 AMSL elevation, with bubble size indicating the monthly standard deviation.

277 **4. Results**

278 **4.1 Waterline detection**

279 Each satellite-derived waterline, and its cross-shore position  $W_{sat}$ , acquired since 2009 was  
 280 systematically compared with the theoretical waterline (cross-shore position  $W\eta$ ) computed using  
 281 the Truc Vert beach survey performed closest to the satellite flyover date. For this, all the proxies of  
 282 water level at the coast  $\eta$  detailed in Section 3.1 were projected on the beach survey. Figure 6 shows  
 283 an example of the Landsat 8 image taken on November 17, 2014, at 10:48 AM GMT, corresponding  
 284 to incident waves with  $H_s = 2.8$  m near mid-high tide ( $\eta_t = 0.76$  m) with negligible non-tidal residuals  
 285 ( $< 0.01$  m) and large runup ( $R_{2\%} = 1.73$  m). CoastSat detects an alongshore non-uniform waterline  
 286 depicting megacusp embayments enforced by the inner-bar rip channels (Figure 6a–c). This cusped  
 287 morphology is also observed on the closest beach topography, which was surveyed three days later  
 288 on February 20, 2019. The  $\eta_o$  ( $\eta = 0$ ) elevation iso-contour is located well offshore of the satellite-  
 289 derived waterline (yellow circles in Figure 6d), on average by c. 70.1 m (Figure 6e). Taking into  
 290 account the astronomical tide, the  $\eta_t$  elevation iso-contour is located closer to the satellite-derived  
 291 waterline (Figure 6d), although still well offshore by c. 43.8 m (Figure 6f). Given the negligible non-  
 292 tidal residuals at the time of this L8 satellite image, the  $\eta_{ts}$  elevation iso-contour essentially  
 293 superimposes onto that of  $\eta_t$  (Figure 6d,g). In contrast, including wave runup the  $\eta_{tsr}$  elevation iso-  
 294 contour is translated landward very close to the satellite-derived waterline (Figure 6d), located  
 295 onshore by c. 2.0 m with an alongshore-averaged root mean square error of 3.7 m (Figure 6h).





296

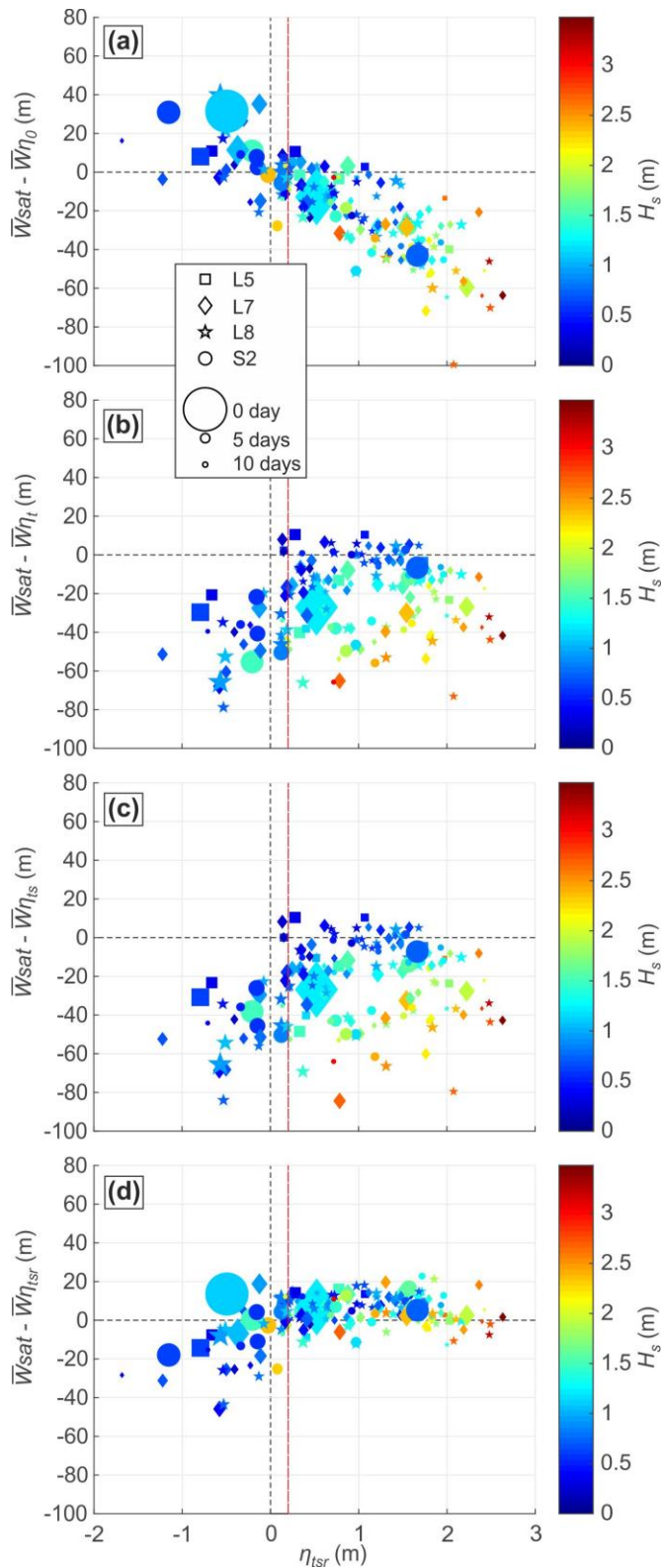
297 Figure 6. (a-c) Outputs from the CoastSat tool of Vos (2019b) from L8 satellite on November 17, 2014  
 298 at 10:48 AM GMT near mid-high tide ( $\eta_t = 0.76$  m) under energetic waves ( $H_s = 2.8$  m) with (a) RGB  
 299 image of Truc Vert beach; (b) output of image classification where each pixel is labelled as ‘sand’,  
 300 ‘water’, ‘white-water’ or ‘other’; and (c) pseudocolor image of the MNDWI pixel values. In (a-c), the  
 301 red box indicates survey region and reference frame used at Truc Vert beach, and the black line  
 302 indicates the CoastSat waterline. (d) Truc Vert beach topographic survey on November 10, 2014, with  
 303 AMSL elevation coloured, superimposed waterline points (magenta dots) detected by CoastSat in (a-  
 304 c) and superimposed iso-contours of elevations:  $\eta_0$  (0 AMSL),  $\eta_t$  (0.76 m),  $\eta_{ts}$  (0.76 m) and  $\eta_{tsr}$  (2.50  
 305 m). Note that the  $\eta_t$  line is hidden behind the  $\eta_{ts}$  line due to negligible non-tidal residual, and that the  
 306  $\eta_{tsr}$  line is partly hidden behind the satellite data points. The dashed black line indicates the 1.5-m  
 307 elevation iso-contour (shoreline proxy at Truc Vert). Comparison of satellite-derived waterline cross-  
 308 shore positions  $W_{sat}$  against cross-shore positions of iso-contours of elevation (e)  $\eta_0$ , (f)  $\eta_t$ , (g)  $\eta_{ts}$  and  
 309 (h)  $\eta_{tsr}$  with corresponding correlation (R), root-mean-square error (RMSE) and difference in means  
 310 (Bias) statistics.

311 Table 1 shows the alongshore-averaged waterline cross-shore position  $\bar{W}\eta$  statistics for all usable  
 312 satellite images since 2009 and for each of the 4 proxies of water level  $\eta$  at the coast. Using all the  
 313 images since 2009 ( $n = 226$ , left-hand column of Table 1), agreement is poor when assuming constant  
 314 water level at the coast (mean sea level  $\bar{W}\eta_0$ ,  $R^2 = 0.06$ , RMSE = 29.0, Bias = -14.9 m). Using  
 315 astronomical tide ( $\bar{W}\eta_t$ ) improves the agreement ( $R^2 = 0.60$ ), while adding the atmospheric surge  
 316 component ( $\bar{W}\eta_{ts}$ ) does not provide further improvement ( $R^2 = 0.59$ ). In all two situations, the  
 317 unbiased RMSE (standard deviation STD) and Bias are however still large (STD > 20 m and Bias < -20  
 318 m). Further adding wave runup to water level iso-contour greatly improves the agreement with  
 319 CoastSat waterline ( $\bar{W}\eta_{tsr}$ ,  $R^2 = 0.84$ , STD = 12.4 m, Bias = 3.1 m). Figure 7 further shows that, not  
 320 surprisingly, errors using  $\eta_0$  increase as the water level at the time of the satellite flyover deviates  
 321 from MSL (Figure 7a). In contrast, using astronomical tide ( $\bar{W}\eta_t$ ), errors are decreased for higher  
 322 water levels due to steeper beach and small wave height due to smaller runup, say  $\eta_{tsr} > 0$  and  $H_s < 1$   
 323 m (Figure 7b), which is the same further adding non-tidal residuals ( $\bar{W}\eta_{ts}$ , Figure 7c). Finally, further  
 324 adding wave runup ( $\bar{W}\eta_{tsr}$ ) shows that alongshore-averaged waterline positions are systematically  
 325 close to that obtained with CoastSat, independent of wave height, for water levels  $\eta_{mr} > 0.2$  m which  
 326 is also where the break in slope occurs (Figure 7d). This is reflected in the statistics provided in the  
 327 middle column of Table 1 for ( $\eta_{tsr} > 0.2$  m,  $n = 164$ ), showing that, while the coefficient of  
 328 determination is slightly decreased, STD drops to 7.0 m. A positive Bias is found (7.1 m, Table 1),  
 329 meaning that the satellite-derived waterline  $\bar{W}^{sat}$  is located landward of the theoretical waterline  
 330  $\bar{W}\eta_{tsr}$ , which will be discussed in Section 5. Interestingly, keeping only high-tide images ( $\eta_t > 0.5$  m  
 331 like in Vos et al., 2019a,  $n = 69$ ), only slightly improves the results (right-hand column of Table 1), but  
 332 more than halves the number of usable images. At the other end (left-hand column of Table 1), using  
 333 all the images results in larger correlation ( $R^2 = 0.84$ ) and smaller RMSE (12.8 m). However, STD is  
 334 almost doubled. These results indicate that, for this study site, using  $\eta_{tsr}$  which includes wave runup  
 335 and selecting images with  $\eta_{tsr} > 0.2$  m is the optimal strategy that both minimizes alongshore-  
 336 averaged waterline position error and maximizes the number of usable satellite images. Finally, it is  
 337 important to note that these comparisons consider satellite images and beach surveys separated by  
 338 up to 10 days (Figure 7). Given the large morphological changes occurring at Truc Vert, the errors  
 339 given here must be considered as conservative.

340 Table 1. Statistics of alongshore-averaged waterline cross-shore positions  $\bar{W}\eta$  for each of the 4 water  
 341 elevation proxies against alongshore-averaged waterline cross-shore position  $\bar{W}^{sat}$  computed with  
 342 CoastSat, using all satellite images, or selecting only those taken for  $\eta_{tsr} > 0.2$  m or  $\eta_t > 0.5$  m. Only  
 343 satellite images for which a beach survey was performed within 10 days were considered.



|                             | All ( $n = 226$ ) |             |                | $\eta_{tsr} > 0.2$ m ( $n = 164$ ) |             |                | $\eta_t > 0.5$ m ( $n = 69$ ) |             |                |
|-----------------------------|-------------------|-------------|----------------|------------------------------------|-------------|----------------|-------------------------------|-------------|----------------|
|                             | RMSE<br>(STD) [m] | Bias<br>[m] | R <sup>2</sup> | RMSE (STD)<br>[m]                  | Bias<br>[m] | R <sup>2</sup> | RMSE (STD)<br>[m]             | Bias<br>[m] | R <sup>2</sup> |
| $\bar{W}_{\eta_0}$<br>(MSL) | 29.0 (24.8)       | -14.9       | 0.06           | 30.7 (17.5)                        | -24.2       | 0.05           | 34.0 (14.1)                   | -30.9       | 0.15           |
| $\bar{W}_{\eta_t}$          | 28.9 (20.2)       | -20.7       | 0.60           | 23.4 (17.1)                        | -16.0       | 0.26           | 14.5 (12.0)                   | -8.1        | 0.28           |
| $\bar{W}_{\eta_{ts}}$       | 31.4 (21.1)       | -23.3       | 0.59           | 26.1 (18.7)                        | -18.2       | 0.23           | 15.5 (12.6)                   | -9.1        | 0.24           |
| $\bar{W}_{\eta_{tsr}}$      | 12.8 (12.4)       | 3.1         | 0.84           | 10.0 (7.0)                         | 7.1         | 0.78           | 10.6 (6.0)                    | 8.7         | 0.80           |



345

346 Figure 7. Difference between alongshore-averaged iso-contour cross-shore position ( $\bar{W}_{\eta}$ ) for

347 elevations (a)  $\eta_0$ , (b)  $\eta_t$ , (c)  $\eta_{ts}$  and (d)  $\eta_{tsr}$  and alongshore-averaged waterline cross-shore position

348 computed with CoastSat  $\bar{W}_{sat}$ , positive meaning more landward satellite-derived waterline, against

349 estimated total water level  $\eta_{tsr}$ . In all panels, significant wave height  $H_s$  is coloured, the vertical

350 dashed red line indicates the  $\eta_{tsr} = 0.2$  m threshold, symbol indicates the satellite and symbol size is

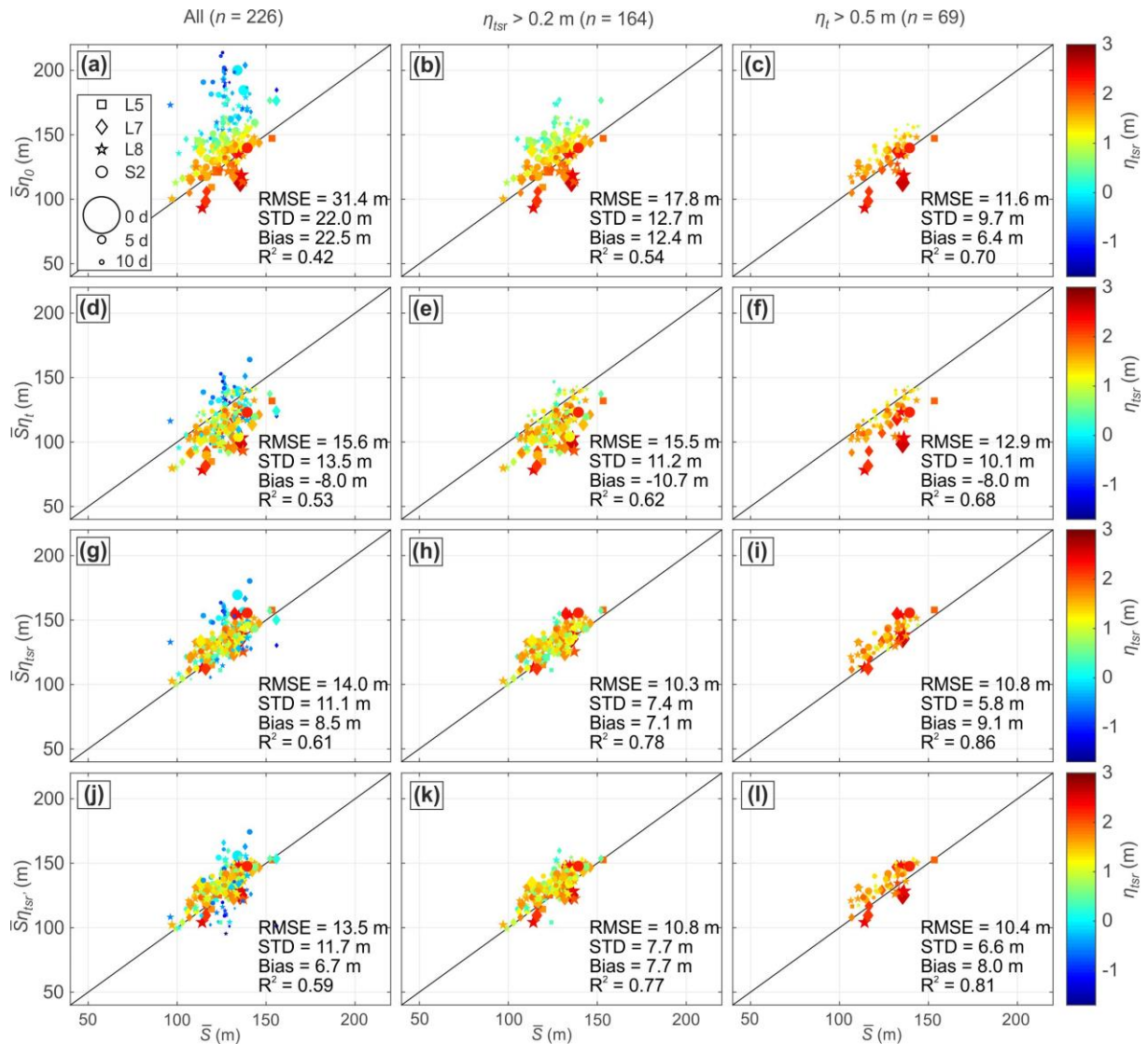
351 proportional to the duration between the satellite image and the closest Truc Vert beach  
352 topographic survey used to compute iso-contours.

#### 353 4.2 Shoreline position

354 Based on the results of the analysis on the role of water level proxies on the alongshore-averaged  
355 waterline cross-shore position  $\bar{W}\eta$ , and to facilitate comparison with earlier work, only four satellite-  
356 derived shoreline position ( $S\eta$ ) methods are further considered by translating horizontally a given  
357 waterline  $W\eta$  using a given beach slope. Below we now disregard elevation  $\eta_{ts}$  as non-tidal residuals  
358 were found to have negligible impact on waterline position at Truc Vert and address four alongshore-  
359 averaged shoreline position: (1)  $\bar{S}\eta_0$  ignoring tide; (2)  $\bar{S}\eta_t$  with tidal correction using water level  $\eta_t$   
360 and a constant slope ( $m = 0.05$  in Equation (2)) as in Vos et al. (2019a); (3)  $\bar{S}\eta_{tsr}$  with tidal correction  
361 using water level  $\eta_{tsr}$  (i.e. including wave runup) and a constant slope  $m = 0.05$  and (4)  $\bar{S}\eta_{tsr}$  with  
362 tidal correction using water level  $\eta_{tsr}$  (i.e. including wave runup) and the time- and elevation-varying  
363 monthly beach slope shown in Figure 5 feeding Equation (2). Figure 8 shows that the poorest  
364 agreement with field data is found for  $\bar{S}\eta_0$  (STD = 22.0 m,  $R^2 = 0.42$ , Figure 8a), although agreement  
365 substantially improves when only considering high-tide images ( $\eta_t > 0.5$  m; STD = 10.9 m,  $R^2 = 0.64$ ,  
366 Figure 8c). Surprisingly enough, using  $\bar{S}\eta_t$  for high-tide images does not further improve the results  
367 (Figure 8f). Although a direct comparison cannot be performed, Vos et al. (2019a) who used 74  
368 satellite-derived shorelines between 2005-2018 for  $\eta_t > 0.5$  m at a single transect at Truc Vert, found  
369 similar results (STD = 12.7 m,  $R^2 = 0.46$ ). In contrast, results dramatically improve for  $\bar{S}\eta_{tsr}$  (STD = 5.8  
370 m,  $R^2 = 0.86$ , Figure 8i), meaning that including runup in water level estimation at this coast is key to  
371 improve the derived shoreline position. It is important to note that similar agreement is obtained  
372 disregarding non-tidal residuals and only including astronomical tide and wave runup (STD = 5.6 m,  $R^2$   
373 = 0.86, not shown).

374 Results are not further improved when using a time- and elevation-varying monthly beach slope  
375  $\bar{S}\eta_{tsr}$  (STD = 6.6 m,  $R^2 = 0.81$ , Figure 8l). This means that, in line with Vos et al. (2019a), further  
376 including a presumably better description of beach slope does not necessarily improve the derived  
377 shoreline position. While the best results are obtained for  $\bar{S}\eta_{tsr}$  for high-tide images, importantly,  
378 performance is only marginally less good by including more than twice as many images for  $\eta_{tsr} > 0.2$   
379 m (STD = 7.4 m,  $R^2 = 0.78$  in Figure 8h). Therefore, using  $\bar{S}\eta_{tsr}$  appears as the optimal approach to  
380 infer shoreline position by both maximizing the number of usable images leading to improved  
381 temporal resolution of the shoreline signal and minimizing spatial error associated with the shoreline  
382 estimates. Importantly, a substantial positive 7.1 m bias is found, meaning that satellite-derived  
383 shoreline is located too far seaward, which will be discussed in Section 5. Disregarding non-tidal

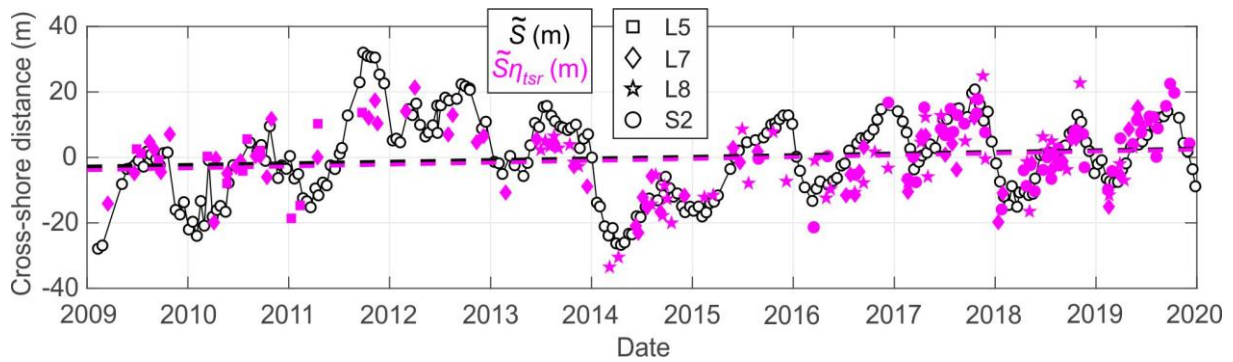
384 residuals and only considering astronomical tide and wave runup ( $\bar{S}\eta_{tsr}$ ) gives similar results (STD =  
 385 7.2 m,  $R^2 = 0.78$  for  $\eta_{tsr} > 0.2$  m, not shown) to  $S\eta_{tsr}$ . This emphasizes that astronomical tide and wave  
 386 runup are key to satellite-derived shorelines, and that, at Truc Vert, non-tidal residuals can be  
 387 disregarded. Finally, as per the waterline detection, all these errors are considered conservative due  
 388 to the comparison window (< 10 days between the satellite image the beach survey used for  
 389 comparison).



390  
 391 Figure 8. Satellite-derived alongshore-averaged shoreline position against in-situ shoreline position  
 392 with corresponding statistics using only satellite images for which a beach survey was performed less  
 393 than 10 days before or after. A positive bias means that satellite-derived shoreline is located too far  
 394 seaward. The analysis includes (left-hand panels) all usable satellite images since 2009 ( $n = 226$ );  
 395 (middle panels) only satellite images for  $\eta_{tsr} > 0.2$  m ( $n = 164$ ); and (right-hand panels) only satellite  
 396 images for  $\eta_t > 0.5$  m ( $n = 69$ ). (a–c)  $\bar{S}\eta_0$ , (d–f)  $\bar{S}\eta_t$ , (g–i)  $\bar{S}\eta_{tsr}$  and (j–l)  $\bar{S}\eta_{tsr}'$ .

397 **4.3 Shoreline change analysis: long term trend and interannual variability**

398 Figure 9 shows the time series of alongshore-averaged shoreline position (1.5 m AMSL elevation  
 399 shoreline proxy) deviation from the mean measured at Truc Vert ( $\tilde{S}$ ) and that derived from satellite  
 400 images  $\tilde{S}_{\eta_{tsr}}$  for images with  $\eta_{mr} > 0.2$  m. The satellite-derived shoreline readily reproduces the  
 401 seasonal and interannual cycles at Truc Vert, despite a few outliers. The computed 2009–2019  
 402 shoreline trends from measurements and satellite are +0.50 m/yr and +0.57 m/yr, respectively,  
 403 therefore showing good agreement. Noteworthy, the trend computed using  $\tilde{S}_{\eta_0}$  ( $n = 226$ ) and  $\tilde{S}_{\eta_t}$  ( $n$   
 404 = 69) is 0.81 m/yr and 0.78 m/yr, respectively, which is substantially larger, but of the same order of  
 405 magnitude as that derived using  $\tilde{S}_{\eta_{tsr}}$  ( $n = 164$ ). Importantly, disregarding non-tidal residuals but  
 406 keeping runup contribution, 2009-2019 shoreline trend of  $\tilde{S}_{\eta_{tr}}$  is 0.63 m/yr, which is closer to that  
 407 computed from the topographic surveys.

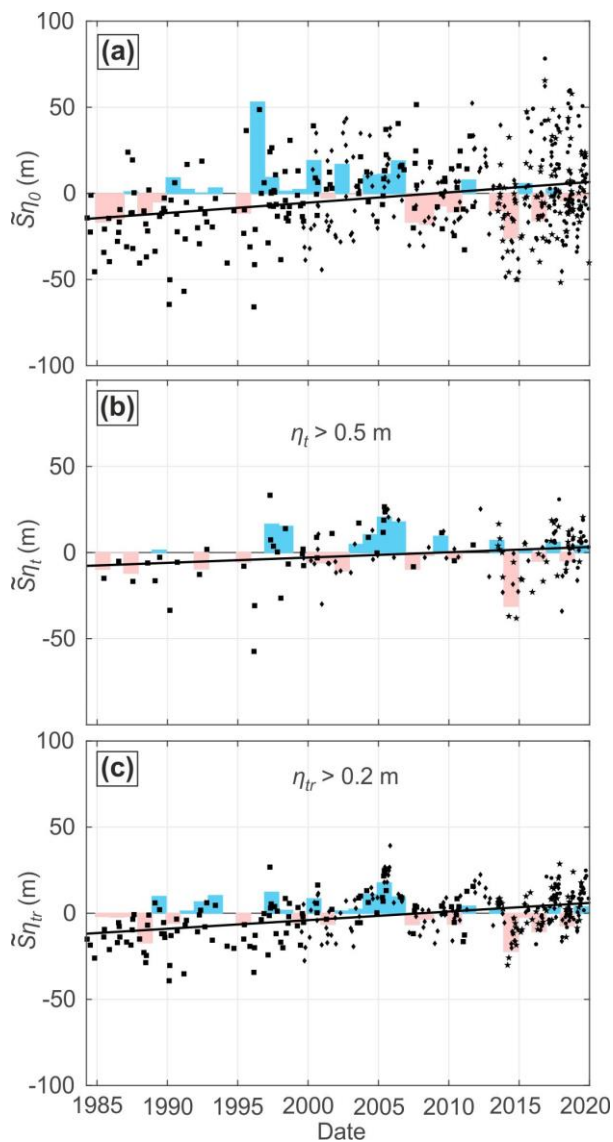


408  
 409 Figure 9. Time-series of shoreline change at Truc Vert beach derived from satellite  $\tilde{S}_{\eta_{tsr}}$  compared  
 410 with in-situ shoreline position  $\tilde{S}$  with superimposed trends (dashed lines).

411 Figure 10 shows the time series of shoreline deviation from the mean for the entire satellite image  
 412 dataset, starting from April 21, 1984. Figure 10b shows the results using our optimal approach, which  
 413 is here disregarding hindcasted non-tidal residuals as they are not available prior to 2006 (and  
 414 including these did not represent significant improvement anyway). The corresponding  $\tilde{S}_{\eta_{tr}}$  long-  
 415 term trend using images with  $\eta_{tr} > 0.2$  m is 0.50 m/yr, which is very similar to that computed for the  
 416 2009-2019 period (Figure 10a). The long-term trend computed with shoreline  $\tilde{S}_{\eta_0}$  is also similar  
 417 (+0.60 m/yr), while that using  $\tilde{S}_{\eta_t}$  for images with  $\eta_t > 0.5$  m is slightly reduced (+0.31 m/yr).

418 To emphasize interannual variability, we computed the yearly post-winter mean shoreline position  
 419 from which we subtracted the long-term trend (coloured bars in Figure 10a). The number of usable  
 420 satellite images increased in time (Figure 3d) from 2 in 1993 and 1994 to 49 in 2018, and also varied  
 421 seasonally, ranging from 0.34 images per year in January to 1.91 images in June (related to cloud  
 422 cover). Therefore, in order to maximize the number of post-winter satellite-derived shoreline  
 423 positions, we systematically averaged all available shoreline data between April and July. Clearly,  
 424 strong interannual variability is highlighted, with a typical amplitude of 30–40 m, and with the

425 2013/2014 winter standing out for all shoreline proxies  $\tilde{S}\eta_{tr}$  (Figure 10b). Interannual cycles are  
 426 more pronounced using  $\tilde{S}\eta_0$  for all images, with a lot of shoreline outliers (Figure 10a). Interannual  
 427 cycles for  
 428  $\tilde{S}\eta_t$  and  $\tilde{S}\eta_{tr}$  are more similar in patterns, although using  $\tilde{S}\eta_t$  for images with  $\eta_t > 0.5$  m does not  
 429 provide enough post-winter data to address interannual variability prior to the 2000s due to the lack  
 430 of available images (Figure 10c). Previous work showed that shoreline inter-annual variability on the  
 431 open beaches of the Atlantic coast of Europe at these latitudes, and particularly at Truc Vert, is  
 432 strongly affected by the WEPA index (Dodet et al., 2019). A high negative correlation ( $R = -0.82$ ) was  
 433 found between post-winter  $\tilde{S}\eta_{tr}$  and winter WEPA index, while correlation drops for  $\tilde{S}\eta_0$  ( $R = -0.50$ )  
 434 and  $\tilde{S}\eta_t$  ( $R = -0.49$ ). This suggests that interannual shoreline variability can be better depicted using  
 435  $\tilde{S}\eta_{tr}$  for  $\eta_{tr} > 0.2$ .



436  
 437 Figure 10. Time-series of satellite-derived shoreline position deviation from the mean at Truc Vert  
 438 beach, with the coloured bars showing the interannual variability (trend removed) in post-winter



439 shoreline position and the solid line depicting long-term trend: (a)  $\tilde{S}\eta_0$  for all images; (b)  $\tilde{S}\eta_t$  for  
440 images with  $\eta_t > 0.5$  m; (c)  $\tilde{S}\eta_{tr}$  for images with  $\eta_{tr} > 0.2$  m.

## 441 5. Discussion and conclusions

442 Our results indicate that, without having to improve the CoastSat satellite-derived waterline  
443 algorithm, the estimation of shoreline position, defined as the profile intersection with a given  
444 elevation datum, can be greatly improved on a meso-macrotidal high-energy sandy beach. Crucial to  
445 this improvement is accounting for the wave runup. This was surprising as it is highly unlikely that  
446 most satellite images were taken at maximum runup excursion. Instead it was expected that the  
447 wave set-up, defined by the time-averaged water level of the waterline would be a better descriptor  
448 of the shoreline position. However, a preliminary analysis showed that wave set-up only slightly  
449 improved waterline detection compared with disregarding wave effects. An explanation for this is  
450 that because beaches such as Truc Vert tend to remain wet after the passage of a single runup event,  
451 the CoastSat algorithm picks-up the interface between the recent runup (wet) and dry sand instead  
452 of the sand/water interface. This may also explain why although the variance in waterline position is  
453 largely accounted for by including the wave runup component, the average position of the resulting  
454 time- and space-averaged waterline is shifted landward by 7.1 m. (Table 1). Improving the waterline  
455 detection for such an environment by using the mean runup instead of the 2% exceedance runup  
456 ( $R_{2\%}$ ) will need further investigation. We also tested other set-up and runup formulas, which did not  
457 yield better results. For instance, the formulation used here by Sénéchal et al. (2011) resulted in a  
458 substantially large inshore bias (runup overestimation) of waterline position compared to other  
459 formulas, meaning that runup elevations are possibly overestimated. However, this formulation  
460 provided the best variance explanation, which is why it was preferred therein. For instance, using  
461 images with  $\eta_{tsr} > 0.2$  m, waterline STD and  $R^2$  are 7.0 m and 0.78 (Table 1), respectively. Results  
462 worsen using the runup parametrizations proposed by Stockdon et al. (2006) for intermediate and  
463 dissipative beaches, with STD = 8.8 m and  $R^2 = 0.67$  for the intermediate beach parametrization, and  
464 with STD = 8.7 m and  $R^2 = 0.67$  for the dissipative parametrization. However, waterline estimation  
465 using Stockdon et al. (2006) is still greatly improved compared with when wave contribution to water  
466 level at the coast is disregarded ( $\bar{W}\eta_0$  and  $\bar{W}\eta_t$  in Table 1). Our new approach also allows using a  
467 lower water level threshold ( $\eta_{tsr} > 0.2$  m), greatly increasing the number of useable images available  
468 for shoreline change analysis. This improvement is especially important for higher latitudes where  
469 more frequent cloud cover significantly reduces the number of cloud-free images. However, this  
470 threshold is likely site specific and does not correspond to any salient break in beach slope at Truc  
471 Vert. Environmental factors controlling this threshold will need to be addressed by exploring  
472 satellite-derived shoreline at other beaches where beach profiles are regularly surveyed.

473 Including the non-tidal water level residuals did not improve the results at Truc Vert. However, this is  
474 not a generic result as at Truc Vert, and along the entire Aquitaine coast studied here (Figure 1a), the  
475 atmospheric surge is quite small (Le Cann, 1990) owing to the quite narrow continental shelf.  
476 Atmospheric surge at Truc Vert at all the satellite flyover dates used here ranged from -0.27 m to  
477 +0.29 m with a mean of -0.05 m (Figure 3e). This is small compared to the wave runup, ranging from  
478 0.17 m to 1.89 m with a mean of 0.91 m (Figure 3f), and the meso-macrotidal tide range (Figure 3e).  
479 However, including storm surge may be critical to improve shoreline estimation on coasts with small  
480 tide range, but potentially large surge due to large and shallow continental shelf. For instance, sea  
481 level can rise by metres due to atmospheric surge in the North Sea (Spencer et al., 2015), the Gulf of  
482 Mexico (Sheng et al., 2004) or even c. 100 km north of the study area where the continental shelf  
483 becomes much wider and shallower (Bertin et al., 2012). For energetic coasts with similar settings as  
484 Truc Vert, overlooking atmospheric surge is acceptable, which is an advantage for practical  
485 applications as accurate local surge hindcasts starting back in the 80s are scarce.

486 Another important parameter to quantify is the beach slope, which is used in traditional set-up and  
487 runup formulas (Stockdon et al., 2006) and for tidal correction (Vos et al., 2019a). Nevertheless, using  
488 a time- and space-varying slope does not improve shoreline reconstruction for Truc Vert, which is  
489 another advantage for practical application as only an average beach slope value needs to be  
490 provided. Recently, Vos et al. (2020) developed a simple and efficient approach to derive beach slope  
491 from the same publicly available satellite images, making it possible to compute satellite shoreline  
492 position without requiring local topographic data.

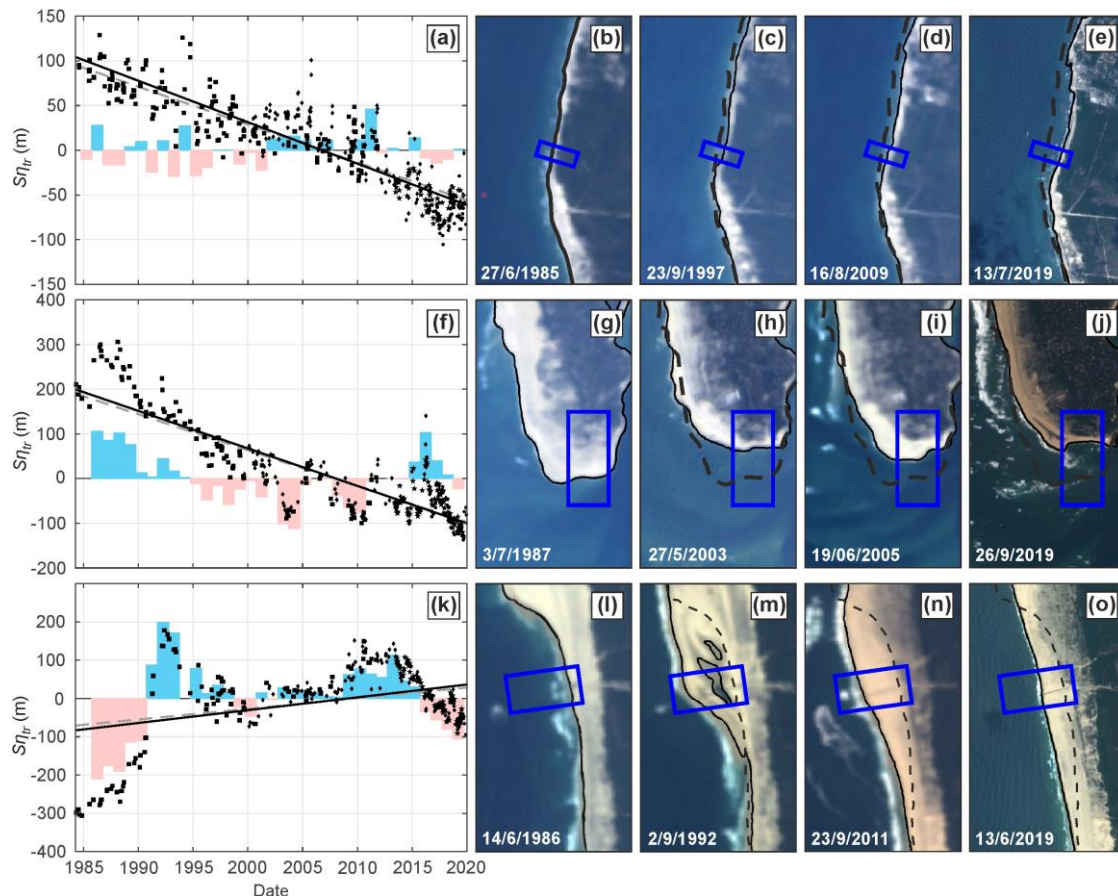
493 Our work has therefore identified key parameters contributing to shoreline error reduction through  
494 the development of a robust methodology. These improvements need to be tested at other sites, in  
495 particular on reflective gravel and mixed sand-gravel beaches, and ultra-dissipative sandy mega-tidal  
496 beaches. Further possibility for uncertainty reduction concerns the georeferencing and the better  
497 detection of the sand/water interface. The CoastSat waterline detection algorithm uses an image  
498 classification based on a Neural Network trained at five beaches along the New South Wales coast  
499 (Vos et al., 2019a). Training a new Neural Network for more representative sites may further improve  
500 the sand/water interface detection. Overall, more work is required to identify and further address  
501 other key sources of uncertainties, which is beyond the scope of the present paper.

502 The 35-year shoreline time series at Truc Vert (1984–2019) shows that more accurate assessment of  
503 long-term shoreline trends and interannual variability can be computed than was achieved in  
504 previous global studies (e.g., Luijendijk et al., 2018; Mentaschi et al., 2018). Similar trends are  
505 obtained with  $\tilde{S}\eta_{tr}$  (+0.50 m/yr) and  $\tilde{S}\eta_0$  (+0.60 m/yr) (Figure 10b). However, shoreline trend



506 computation at other sites along the Aquitaine coast (e.g. Hourtin, Biscarrosse, Figure 1a) indicates  
507 that much larger differences can be observed.  $\tilde{S}\eta_0$ , which does not account for water level  
508 fluctuations, is close to the global approach in Luijendijk et al. (2018) who used yearly composite and  
509 therefore averaged water level variations. A detailed inspection of the trends computed in Luijendijk  
510 et al. (2018) at Truc Vert shows trends that are very different to those computed herein. The  
511 dominant trend computed by Luijendijk et al. (2018) at Truc Vert indicates, strongly alongshore  
512 variable, large, erosion at -1.13 m/yr averaged over the same 3500-m sector, peaking locally at 3.8  
513 m/yr. A strong alongshore variability was also found in Mentaschi et al. (2018), although a direct  
514 quantitative comparison could not be performed. This goes against decadal and multi-decadal  
515 observations at this coast (e.g., Castelle et al., 2017a, 2018) and results presented herein, which all  
516 concur to an alongshore-uniform c. +0.5 m/yr trend. It must be acknowledged that the comparison  
517 above is performed between a site-specific analysis where the images were manually selected and a  
518 runup correction was applied using a local wave and water level hindcast (our study), and a global  
519 method that was applied over the whole world (Luijendijk et al., 2018; Mentaschi et al., 2018).

520 We therefore anticipate that the new approach proposed here can improve the accuracy of satellite  
521 shoreline long-term trends and interannual variability along many coasts worldwide. However, at  
522 rapidly evolving sections, improvements will be marginal. North of Truc Vert, at Cape Négade (Figure  
523 1a), the long-term trend is reasonably steady at -4.63 m/yr for  $\tilde{S}\eta_{tr}$  (Figure 11a-e), and is very similar  
524 with all the other shoreline proxies (not shown). The same applies further south at the tip of the Cap  
525 Ferret sand spit or at La Salie at each side of the Arcachon Lagoon tidal inlet, where large long-term  
526 trends of +3.34 m/yr and -8.38 m/yr are computed, respectively. However, large cycles are observed  
527 with some dramatic decadal trends. For instance, the shoreline at La Salie has been eroding by nearly  
528 30 m/yr over the last seven years (Figure 11k), despite an overall positive shoreline trend since the  
529 1980s. Therefore, except at Cape Négade, where chronic erosion is relatively steady, further  
530 extrapolating these 35-year trends to estimate shoreline position by 2100 (Vousdoukas et al., 2020)  
531 is questionable, because time scales of shoreline cycles are similar to the period of satellite data  
532 availability.



533

534 Figure 11. Left-hand panels: time series of shoreline position at (a) Cape Négade, (f) Cap Ferret  
 535 sandspit tip and (k) la Salie (see location map in Figure 1a) derived from satellite  $\tilde{S}\eta_{tr}$ . In the left-  
 536 hand panels the linear shoreline trend for  $\tilde{S}\eta_{tr}$  is indicated by the black dotted line. The coloured  
 537 bars in (a,b) show the inter-annual variability (trend removed) in post-winter shoreline position.  
 538 Right-hand panels: corresponding RGB images at different relevant stages of evolution, blue boxes  
 539 indicate areas where shoreline positions were averaged alongshore to compute the time series  
 540 shown in the left-hand panels.

541 We acknowledge that the concept of global application is very attractive and responds to strong  
 542 demand. However, past shoreline trends estimations on beaches incurs large uncertainties, which  
 543 become exacerbated if extrapolated in time to estimate future shoreline change. Vos et al. (2019a)  
 544 recognised issues with dissipative and large tidal range sites. This work has identified key parameters  
 545 contributing to large errors for this type of environment and developed a robust methodology for  
 546 limiting uncertainty. Such approach requires accurate tide and inshore wave hindcasts, which can be  
 547 challenging to obtain in complex coastal settings where, e.g., wave shadowing from offshore islands  
 548 or offshore wave refraction can largely impact breaking wave conditions. These improvements need  
 549 to be tested in other sites with similar tidal/wave forcing characteristics but different morphological  
 550 and sediment characteristics. This will allow addressing the links between coastal response and large-

551 scale climate patterns of atmospheric variability in a wide range of environments. It will also provide  
552 improved beach state classification and, where time scales of shoreline cycles are not similar to the  
553 period of data availability (e.g. away from inlet and estuary mouths), less uncertain shoreline  
554 projections by the end of the century in the context of climate change.

## 555 **Acknowledgments**

556 BC, VM and SB funded by Agence Nationale de la Recherche (ANR) grant number ANR-17-CE01-0014;  
557 GM and TS funded by the NERC BLUEcoast project (NE/N015525/1); CS and AK funded by Coastal and  
558 Marine Applied Research. This study includes the monitoring site of Truc Vert labelled by the Service  
559 National d'Observation (SNO) Dynalit (<https://www.dynalit.fr>). The Observatoire de la Côte Aquitaine  
560 (OCA) and Observatoire Aquitain des Sciences de l'Univers (OASU) provide additional financial  
561 support for the surveys. NORFAS-UG wave hindcast data provided by LOPS-Ifrermer. French Centre  
562 d'Archivage National de Données de Houle In Situ (CANDHIS) buoy network operated by French  
563 Centre d'Etudes et d'expertise sur les Risques, l'Environnement, la Mobilité et l'Aménagement  
564 (CEREMA). GM and TS were supported and partly funded by the UK Natural Environment Research  
565 Council (NE/M004996/1; BLUE-coast project). CS and AK were supported by the Coastal and Marine  
566 Applied Research consultancy.

## 567 **References cited**

- 568 Almar, R., Castelle, B., Ruessink, B.G., Sénéchal, N., Bonneton, P., Marieu, V., 2010. Two- and three-  
569 dimensional double-sandbar system behaviour under intense wave forcing and a meso-  
570 macro tidal range. *Continental Shelf Research*, 30, 781-792.
- 571 Baptista, P., Bastos, L., Bernardes, C., Cunha, T., Dias, J., 2008. Monitoring Sandy Shores  
572 Morphologies by DGPS—A Practical Tool to Generate Digital Elevation Models. *Journal of*  
573 *Coastal Research*, 24, 1516–1528, doi:10.2112/07-0861.1.
- 574 Bertin, X., Bruneau, N., Breilh, J.F., Fortunato, A.B., Karpytchev, M., 2012. Importance of wave age  
575 and resonance in storm surges: The case Xynthia, Bay of Biscay. *Ocean Modelling*, 42, 16-30,  
576 doi:10.1016/j.ocemod.2011.11.001.
- 577 Boudière, E., Maisondieu, C., Arduin, F., Accensi, M., Pineau-Guillou, L., Lepesqueur, J., 2013. A  
578 suitable metocean hindcast database for the design of Marine energy converters.  
579 *International Journal of Marine Energy*, 3–4, 40-52, doi:10.1016/j.ijome.2013.11.010
- 580 Carter, R.W.G., Johnston, T.W., McKenna, J., Orford, J.D., 1987. Sea-level, sediment supply and  
581 coastal changes: Examples from the coast of Ireland. *Progress In Oceanography*, 18(1-4), 79-  
582 101.

583 Castelle, B., Bonneton, P., Dupuis, H., Sénéchal, N., 2007. Double bar beach dynamics on the high-  
584 energy meso-macrotidal French Aquitanian Coast: a review. *Marine Geology*, 245, 141-159.

585 Castelle, B., Marieu, V., Bujan, S., Ferreira, S., Parisot, J.P., Capo, S., Senechal, N., Chouzenoux, T.,  
586 2014. Equilibrium shoreline modelling of a high-energy meso-macrotidal multiple-barred  
587 beach. *Marine Geology*, 347, 85–94.

588 Castelle, B., Bujan, S., Ferreira, S., Dodet, G., 2017a. Foredune morphological changes and beach  
589 recovery from the extreme 2013/2014 winter at a high-energy sandy coast. *Marine Geology*,  
590 385, 41-55.

591 Castelle, B., Dodet, G., Masselink, G., Scott, T., 2017b. A new climate index controlling winter wave  
592 activity along the Atlantic coast of Europe: The West Europe Pressure Anomaly. *Geophysical*  
593 *Research Letters*, 44 (3), 1384-1392.

594 Castelle, B., Guillot, B., Marieu, V., Chaumillon, E., Hanquiez, V., Bujan, S., Poppeschi, C., 2018. Spatial  
595 and temporal patterns of shoreline change of a 280-km long high-energy disrupted sandy  
596 coast from 1950 to 2014: SW France. *Estuar. Coast. Shelf Sci.* 200, 212–223.

597 Castelle, B., Marieu, V., Bujan, S., Ferreira, S., 2020. 16 years of topographic surveys of rip-channelled  
598 high-energy meso-macrotidal sandy beach. *Scientific Data*, 7, 410, doi:10.1038/s41597-020-  
599 00750-5.

600 Cipolletti, M.P., Delrieux, C.A., Perillo, G.M.E., Cintia Piccolo, M., 2012. Superresolution border  
601 segmentation and measurement in remote sensing images. *Comput. Geosci.*, 40, 87–96,  
602 doi:10.1016/j.cageo.2011.07.015.

603 Cooper, J. A.G., Masselink, G., Coco, G., Short, A.D., Castelle, B., Rogers, K., Anthony, E., Green, A.N.,  
604 Kelley, J.T., Pilkey, O.H., Jackson, D.W.T., 2020. Sandy beaches can survive sea-level rise.  
605 *Nature Climate Change*, 10 (11), 993-995, doi:10.1038/s41558-020-00934-2.

606 D’Anna, M., Castelle, B., Idier, D., Le Cozannet, G., Rohmer, J., Robinet, A., 2020. Impact of model free  
607 parameters and sea-level rise uncertainties on 20-years shoreline hindcast: the case of Truc  
608 Vert beach (SW France). *Earth Surface Processes and Landforms*, 45(8), 1895-1907,  
609 doi:10.1002/esp.4854

610 Dodet, G., Castelle, B., Masselink, G., Scott, T., Davidson, M., Floc’h, F., Jackson, D.W.T., Suanez, S.,  
611 2019. Beach recovery from extreme storm activity during the 2013/14 winter along the  
612 Atlantic coast of Europe. *Earth Surface Processes and Landforms*, 44(1), 393-401.

613 Duarte, C.R., De Miranda, F.P., Landau, L., Souto, M.V.S., Sabadia, J.A.B., Da Silva, C.A., Rodrigues,  
614 L.I.D.C., Damasceno, A.M., 2018. Short-time analysis of shoreline based on RapidEye satellite  
615 images in the terminal area of Pecem Port, Ceara, Brazil. *International Journal of Remote*  
616 *Sensing*, 39, 4376-4389.

617 Gallagher, E.L., MacMahan, J.H., Reniers, A.J.H.M., Brown, J., Thornton, E.B., 2011. Grain size  
618 variability on a rip-channeled beach. *Marine Geology* 1-4, 43–53.

619 Garcia-Rubio, G., Huntley, D., Russell, P., 2015. Evaluating shoreline identification using optical  
620 satellite images. *Marine Geology*, 359, 96-105, doi:10.1016/j.margeo.2014.11.002.

621 Harley, M.D., Turner, I.L., Short, A.D., Ranasinghe, R., 2011. Assessment and integration of  
622 conventional, RTK-GPS and image-derived beach survey methods for daily to decadal coastal  
623 monitoring. *Coastal Engineering* 58, 194–205.

624 Harley, M.D., Turner, I.L., Kinsela, M.A., Middleton, J.H., Mumford, P.J., Splinter, K.D., Phillips, M.S.,  
625 Simmons, J.A., Hanslow, D.J., Short, A.D., 2017. Extreme coastal erosion enhanced by  
626 anomalous extratropical storm wave direction. *Scientific Reports*, 7: 6033.

627 Hurrell, J.W., 1995. Decadal Trends in the North Atlantic Oscillation: Regional Temperatures and  
628 Precipitation. *Science*, 269, 676-679.

629 Ibaceta, R., Splinter, K.D., Harley, M.D., & Turner, I.L., 2020. Enhanced Coastal Shoreline Modeling  
630 Using an Ensemble Kalman Filter to include Nonstationarity in Future Wave Climates.  
631 *Geophysical Research Letters*, 47(22), doi.org/10.1029/2020GL090724

632 Laporte-Fauret, Q., Marieu, V., Castelle, B., Michalet, R., Bujan, S., Rosebery, D., 2019. Low-Cost UAV  
633 for High-Resolution and Large-Scale Coastal Dune Change Monitoring Using  
634 Photogrammetry. *Journal of Marine Science Engineering*, 7:63, doi: 10.3390/jmse7030063.

635 Le Cann, B., 1990. Barotropic tidal dynamics of the Bay of Biscay shelf: observations, numerical  
636 modelling and physical interpretation. *Continental Shelf Research*, 10 (8), 723–758.

637 Lee, G.H., Nicholls, R.J., Birkemeier, W.A., 1998. Storm-driven variability of the beach-nearshore  
638 profile at Duck, North Carolina, USA, 1981–1991. *Mar. Geol.* 148 (3), 163–177.

639 Le Mauff, B., Juigner, M., Ba, A., Robin, M., Launeau, P., Fattal, P., 2018. Coastal monitoring solutions  
640 of the geomorphological response of beach-dune systems using multi-temporal LiDAR  
641 datasets (Vendée coast, France), *Geomorphology*, 304,121-140, doi  
642 :10.1016/j.geomorph.2017.12.037.

643 Liu, Q., Trinder, J., Turner, I.L., 2017. Automatic super-resolution shoreline change monitoring using  
644 Landsat archival data: a case study at Narrabeen–Collaroy Beach, Australia. *Journal of*  
645 *Applied Remote Sensing*, 11, 016036, doi:10.1117/1.JRS.11.016036.

646 Luijendijk, A., Hagenaaars, G., Ranasinghe, R., Baart, F., Donchyts, G., Aarninkhof, S., 2018. The State  
647 of the World’s Beaches. *Scientific Reports*, 8(1), doi:10.1038/s41598-018-24630-6.

648 Ludka, B.C., Guza, R.T., O’Reilly, W.C., Merrifield, M.A., Flick, R.E., Bak, A.S., Hesser, T., Bucciarelli, R.,  
649 Olfe, C., Woodward, B., Boyd, W., Smith, K., Okihiro, M., Grenzeback, R., Parry, L., Boyd,  
650 G., 2019. Sixteen years of bathymetry and waves at San Diego beaches. *Sci Data* 6, 161,  
651 doi:10.1038/s41597-019-0167-6.

652 McCarroll, R.J., Masselink, G., Valiente, N.G., Scott, T., Wiggins, M., Kirby, J., Davidson, M., 2020. A  
653 novel rules-based shoreface translation model for predicting future coastal change:  
654 ShoreTrans. Doi:10.31223/osf.io/y4kmv

655 Masselink, G., Castelle, B., Scott, T., Dodet, G., Suanez, S., Jackson, D., Floc'h, F., 2016. Extreme wave  
656 activity during 2013/2014 winter and morphological impacts along the Atlantic coast of  
657 Europe. *Geophysical Research Letters*, 43, 2135-2143, doi: 10.1002/2015GL067492.

658 Mentaschi, L., Vousdoukas, M.I., Pekel, J.-F., Voukouvalas, E., Feyen, L., 2018. Global long-term  
659 observations of coastal erosion and accretion. *Scientific Reports*, 8, 12876,  
660 doi:10.1038/s41598-018-30904-w.

661 Michaud, H., Pasquet, A., Baraille, R., Leckler, F., Aouf, L., Dalphinnet, A., Huchet, M., Roland, A.,  
662 Dutour-Sikiric, M., Ardhuin, F., Filipot, J.F., 2015. Implementation of the new French  
663 operational coastal wave forecasting system and application to a wave-current interaction  
664 study. 14th International Workshop on Wave Hindcasting and Forecasting & 5th Coastal  
665 Hazard Symposium, Nov. 8-13, Key West, Florida, USA.

666 Nicolae-Lerma, A., Ayache, B., Ulvoas, B., Paris, F., Bernon, N., Bultreau, T., Mallet, C., 2019.  
667 Pluriannual beach-dune evolutions at regional scale: Erosion and recovery sequences analysis  
668 along the Aquitaine coast based on airborne LiDAR data. *Continental Shelf Research*. 189,  
669 103974.

670 O'Connor, M.C., Cooper, J.A.G., Jackson, D.W.T., 2017. Decadal behavior of tidal inlet-associated  
671 beach systems, Northwest Ireland, in relation to climate Forcing. *Journal of Sedimentary  
672 Research*, 81 (1), 38–51. doi: 10.2110/jsr.2011.3.

673 Pianca, C., Holman, R.A., Siegle, E., 2015. Shoreline variability from days to decades: Results of long-  
674 term video imaging. *Journal of Geophysical Research-Oceans*, 120, 2159–2178.

675 Pineau-Guillou, L., 2013. PREVIMER. Validation des modèles hydrodynamiques 2D des côtes de la  
676 Manche et de l'Atlantique. ODE/DYNECO/PHYSED/2013-05.  
677 <https://archimer.ifremer.fr/doc/00157/26800/>

678 Qiao, G., Mi, H., Wang, W., Tong, X., Li, Z., Li, T., Liu, S., Hong, Y., 2018. 55-year (1960–2015)  
679 spatiotemporal shoreline change analysis using historical DISP and Landsat time series data in  
680 Shanghai, *International Journal of Applied Earth Observation*, 68, 238-251, doi:  
681 10.1016/j.jag.2018.02.009.

682 Ranasinghe, R., Callaghan, D. Stive, M.J.F., 2012. Estimating coastal recession due to sea level rise:  
683 beyond the Bruun rule. *Clim. Chan.*, 110, 561-574.

684 Robinet, A., Castelle, B., Idier, D., Le Cozannet, G., Déqué, M., Charles, E., 2016. Statistical modeling  
685 of interannual shoreline change driven by North Atlantic climate variability spanning 2000-  
686 2014 in the Bay of Biscay. *Geo-Marine Letters*, 36, 479-490.

687 Ruessink, B.G., Kleinhans, M.G., Van den Beukel, P.G.L., 1998. Observations of swash under highly  
688 dissipative conditions. *Journal of Geophysical Research*, 103, 3111-3118.

689 Ruggiero, P., Komar, P.D., Marra, J.J., McDougal, W.G., Beach, R.A., 2001. Wave runup, extreme  
690 water levels and the erosion of properties backing beaches. *Journal of Coastal Research*, 17,  
691 407-419.

692 Schubert, A., Miranda, N., Geudtner, D., Small, D., 2017. Sentinel-1A/B Combined Product  
693 Geolocation Accuracy. *Remote Sensing*, 9(6), 607, doi:10.3390/rs9060607.

694 Senechal, N., Coco, G., Bryan, K.R., and Holman, R.A., 2011. Wave runup during extreme storm  
695 conditions, *Journal of Geophysical Research*, 116, C07032, doi:10.1029/2010JC006819.

696 Sheng, Y.P., Zhang, Y., Paramygin, V.A., 2004. Simulation of storm surge, wave, and coastal  
697 inundation in the Northeastern Gulf of Mexico region during Hurricane Ivan in 2004. *Ocean  
698 Modelling*, 35(4), 314-331, doi:/10.1016/j.ocemod.2010.09.004.

699 Spencer, T., Brooks, S.M., Evans, B.R., Tempest, J.A., Möller, I., 2015. Southern North Sea storm surge  
700 event of 5 December 2013: Water levels, waves and coastal impacts. *Earth-Science Reviews*,  
701 146, 120-145, doi:10.1016/j.earscirev.2015.04.002.

702 Splinter, K., Turner, I.L., Davidson, M.A., 2013. How much data is enough? The importance of  
703 morphological sampling interval and duration for calibration of empirical shoreline models.  
704 *Coastal Engineering*, 77, 14-27, doi:10.1016/j.coastaleng.2013.02.009

705 Splinter, K.D., Turner, I.L., Davidson, M.A., Barnard, P., Castelle, B., Oltman-Shay, J., 2014. A  
706 generalized equilibrium model for predicting daily to interannual shoreline response. *Journal  
707 of Geophysical Research - Earth Surface*, 119, 1936–1958, doi:10.1002/2014JF003106.

708 Stive, M.J.F., Aarninkhof, S.G.J., Hamm, L., Hanson, H., Larson, M., Wijnberg, K.M., Nicholls, R.J.,  
709 Capobianco, M., 2002. Variability of shore and shoreline evolution. *Coastal Engineering*,  
710 47(2), 211-235, doi:10.1016/S0378-3839(02)00126-6.

711 Stockdon, H.F., Holman, R.A., Howd, P.A., Sallenger, A.H., 2006. Empirical parameterization of setup,  
712 swash, and runup. *Coastal Engineering*, 53, 573–588, doi:10.1016/j.coastaleng.2005.12.005.

713 Stokes, C., Davidson, M. Russell, P., 2015. Observation and prediction of three-dimensional  
714 morphology at a high-energy macrotidal beach. *Geomorphology* 243, 1–13.

715 Suanez, S., Cariolet, J.M., Cancouët, R., Ardhuin, F., Delacourt, C., 2012. Dune recovery after storm  
716 erosion on a high-energy beach: Vougot Beach, Brittany (France). *Geomorphology*, 139–140,  
717 16-33, doi:10.1016/j.geomorph.2011.10.014.

718 Toimil, A., Camus, P., Losada, I.J., Le Cozannet, G., Nicholls, R., Idier, D., Maspataud, A., 2020. Climate  
719 change-driven coastal erosion modelling in temperate sandy beaches methods and  
720 uncertainty treatment. *Earth Science Reviews*, 202, 103110,  
721 doi:10.1016/j.earscirev.2020.103110.

722 Toure, S., Diop, O., Kpalma, K., Maiga, A.S., 2019. Shoreline Detection using Optical Remote Sensing:  
723 A Review. *ISPRS Int. J. Geo-Inf.*, 8(2), 75, doi:10.3390/ijgi8020075.

724 Turner, I.L., 2006. Discriminating Modes of Shoreline Response to Offshore-Detached Structures.  
725 *Journal of Waterway, Port, Coastal, and Ocean Engineering*, 132(3), 180-191.

726 Turner, I.L., Harley, M.D., Short, A.D., Simmons, J.A., Bracs, M.A., Phillips, M.S., Splinter, K.D., 2016. A  
727 multi-decade dataset of monthly beach profiles and inshore wave forcing at Narrabeen,  
728 Australia. *Scientific Data*, 2, 160024.

729 Vitousek, S., Barnard, P.L., Limber, P., Erikson, L., Cole, B., 2017. A model integrating longshore and  
730 cross-shore processes for predicting long-term shoreline response to climate change. *Journal*  
731 *of Geophysical Research Earth Surface*, 122, 782– 806, doi:10.1002/2016JF004065.

732 Vos, K., Harley, M.D., Splinter, K.D., Simmons, J.A., Turner, I.L., 2019a. Sub-annual to multi-decadal  
733 shoreline variability from publicly available satellite imagery. *Coastal Engineering*,  
734 doi:10.1016/j.coastaleng.2019.04.004.

735 Vos, K., Splinter, K.D., Harley, M.D., Simmons, J.A., Turner, I.L., 2019b. CoastSat: A Google Earth  
736 Engine-enabled Python toolkit to extract shorelines from publicly available satellite imagery.  
737 *Environmental Modelling & Software*, 122, 104528, doi:10.1016/j.envsoft.2019.104528.

738 Vos, K., Harley, M.D., Splinter, K.D., Walker, A., Turner, I.L., 2020. Beach Slopes From Satellite-Derived  
739 Shorelines. *Geophysical Research Letters*, 47, e2020GL088365, doi:10.1029/2020GL088365

740 Vousdoukas, M.I., Ranasinghe, R., Mentaschi, L., Plomartis, T.A., Athanasiou, P., Luijendyk, A., Feyen,  
741 L., 2020. Sandy Beaches under threat of erosion. *Nature Climate Change*, 10, 260-263,  
742 doi:10.1048/s41558-020-0697-0.

743 Wijnberg, K.M. & Terwindt, J.H., 1995. Extracting decadal morphological behaviour from high-  
744 resolution, long-term bathymetric surveys along the Holland coast using eigenfunction  
745 analysis. *Marine Geology* 126, 301–330.

746 Wiggins, M., Scott, T., Masselink, G., Russell, P., McCarroll, R.J., 2019. Coastal embayment rotation:  
747 Response to extreme events and climate control, using full embayment surveys.  
748 *Geomorphology*, 327, 385-403, doi:10.1016/j.geomorph.2018.11.014.

749 Xu, H., 2006. Modification of normalised difference water index (NDWI) to enhance open water  
750 features in remotely sensed imagery. *Int. J. Remote Sens.* 27, 3025–3033,  
751 doi:10.1080/01431160600589179.